1986A&A...154..154G

Astron. Astrophys. 154, 154–170 (1986)

ASTRONOMY
AND
ASTROPHYSICS

Emission of Lyman α radiation by solar coronal loops

I. General synopsis

P. Gouttebroze[1], J.C. Vial[1] and G. Tsiropoula[2]

[1] Laboratoire de Physique Stellaire et Planétaire, B.P. n° 10, F-91371 Verrières le Buisson Cedex, France
[2] Section of Astrophysics, Astronomy and Mechanics, Department of physics, University of Athens, Athens 15771, Greece

Received April 4, accepted July 2, 1985.

Summary. The processes of emission of Lyman – α radiation by loop-like structures embedded in the solar corona are investigated, for a large range of physical conditions within these objects. The coupled set of equations for radiative transfer, and hydrogen atom level populations, ionization and pressure equilibria is solved to obtain the emitted Lα intensities as functions of pressure, temperature and size. Three different cases are treated: (i) optically thin structures with arbitrary geometry. (ii) plane-parallel slabs, either horizontal or vertical, with arbitrary optical depth. (iii) cylindrical loops with horizontal axis, for moderate optical depths ($\tau < 1000$). The importance of geometry, as well as that of partial frequency redistribution and of the hydrogen atom's model, are evaluated. Empirical formulae and diagrams of intensity as a function of physical state parameters are given. The diagnostic possibilities of Lyman – α filtergrams, alone or in conjunction with other observations, are discussed.

Key words: Sun – Corona – Lyman-α – Loops.

1. Introduction

The highly structured topography of the outer solar atmosphere has been long recognized (Van de Hulst, 1953) and also observed during solar eclipses (Dunn, 1971). However, it is only in the past few years that, with the advent of high spatial resolution space telescopes, the general character of this complex structuring has been confirmed by observations on the sun's disk. A few dedicated X-ray observations were carried out by rocket-borne instruments (Vaiana, 1968), but with the high resolution photographs obtained by the E.U.V. and X-ray instruments on board Skylab during the 1973 – 1974 missions (Vaiana et al., 1973; Tousey et al., 1973) it is readily seen that the basic structures of the corona are loops of various sizes, densities, temperatures and lifetimes, present both inside and outside active regions. These observations concern principally high temperature loops. However, Foukal (1975, 1976, 1978) analyzing the E.U.V. observations obtained with the HCO spectrometer onboard Skylab found that ions characteristic of lower temperatures (typical of the transition region), such as C II, C III, O IV, O V, O VI, can, in some instances, be observed throughout loop structures, even at coronal heights.

During an eclipse in 1970, Gabriel et al. (1971), observed for the first time an intense Lyman - α emission in the corona and the upper chromosphere. Gabriel (1971) interpreted this emission as due to resonance scattering of chromospheric Lα photons by neutral hydrogen atoms present in the coronal plasma.

More recently disk filtergrams in Lα ± 40 Å have been obtained with the "Transition Region Camera" (T.R.C.), a rocket-borne telescope with a spatial resolution of about 1 arcsec (Bonnet et al., 1980). These filtergrams revealed numerous loops, which can be seen in emission at the limb and either in emission or in absorption over the disk (Bonnet and Tsiropoula, 1982). The particular interest of these Lα observations lies in the fact that:

1. Hydrogen is the most abundant element in the solar atmosphere,
2. Among lines of neutral atoms, Lα is the most intense.

Thus, Lα is the most sensitive tool to investigate low temperature components of the upper solar atmosphere.

One of the principal purposes of this paper is to set the basis of a theory that can be applied to the analysis of Lα filtergrams such as those obtained with the TRC. In these observations, the fundamental measurable quantity is the intensity integrated over frequency in a bandpass including the core and the near wings of the line. For observational reasons, it is convenient to use relative, rather than absolute, intensities so that in the following we shall express the Lα intensity of a structure as a dimensionless parameter, the "Lyman-α relative intensity" (LRI), defined as the ratio of the intensity (emitted by that structure) integrated over a 10 nm bandpass around line center, to the same quantity averaged over the solar disk. Since the intensity decreases by several orders of magnitude from the center to the wings, the precise knowledge of the bandpass is not critical, and different observations can be used to determine the value of the two terms of this ratio. The aim of this paper is to establish, for diagnostic purposes, what empirical relationships, if any, may exist between the LRI and the physical variables (temperature, pressure) of relatively cool structures embedded in the corona, observed on or outside the disk. In a forthcoming paper, an analysis of Lyman – α filtergrams, obtained with the T.R.C., will be presented.

This study is divided in three cases, in order to cover the useful ranges of temperature and pressure for coronal structures that may be observed in Lα. These are:

(i) *Optically thin objects* (i.e. high temperature or low pressure loops). As no optically thick transfer problem is involved in this case, solutions may be carried out for arbitrary geometries.

(ii) *Plane-parallel slabs.* A set of equations, including radiative transfer in line and continua, pressure, ionization and level population equilibria, is solved in a self-consistent way. We examine both the case of an horizontal slab, representative of

© European Southern Observatory • Provided by the NASA Astrophysics Data System

1986A&A...154..154G

observations at the center of the solar disk, and that of a vertical slab, related to observations at the limb. The full range of useful optical thicknesses is envisaged.

(iii) *Cylindrical objects.* Here we try to get closer to the actual geometry of observed loops. Comparison of results with those of the preceding case allows an evaluation of the importance of geometrical effects and thus provides a check on the usefulness of plane-parallel computations.

2. Optically thin objects

Here, the structure is assumed to be optically thin in Lα, which ensures the uniformity of the radiation field for every transition of the hydrogen atom, since their absorption coefficients are smaller than that of Lα. Thus, radiative bound-bound rates and photoionization rates are constant throughout the object. Furthermore, the temperature and pressure are assumed constant, which ensures the uniformity of collisional and recombination rates. This last condition is not as restrictive at it may seem, since it is possible to bring several constant-property pieces together to model a more complex structure, such as a sheathed loop, for instance. This uniformity of all rates automatically yields, through the statistical equilibrium equations, that the level populations, absorption coefficients and source functions are also uniform.

2.1. Formulation

2.1.1. Statistical equilibrium

Our model atom includes 3 levels and a continuum. Thus 6 transitions are taken into account: the Lα, Lβ and Hα lines, and the Lyman, Balmer and Paschen continua. For given values of the pressure and the temperature, we compute the transition probabilities as indicated below, and determine the densities of atoms in the different levels by solving the set of the 4 linear equations of statistical equilibrium (including particle conservation). In particular, the number density of atoms in the fundamental state (N_1) yields the Lα absorption coefficient and thus the optical thickness along the line of sight, once the dimensions of the structure are fixed.

2.1.2. Radiative bound-bound rates

The principle of calculation is the same for the 3 lines: we consider optically thin structures lying at low altitude above the solar surface. Therefore, the intensities in the $2\pi\,sr$ outward solid angle may be determined from observations, while they are zero in the opposite half-space (towards the center of the sun). By averaging these intensities over 4π, we get the mean intensity J_ν as a function of the frequency in the line. For Lα and Lβ, intensities are taken from data obtained with the OSO-8/L.P.S.P. experiment. The Lα intensities have been adjusted to obtain a frequency-integrated *outward* intensity (i.e. twice the mean intensity) of $6.55\,10^4$ erg s^{-1} cm^{-2} sr^{-1} (see Lemaire et al., 1981 and references therein). For Hα intensities, we used solar irradiance tables by Beckers et al. (1976). Since radiative excitation probabilities depend linearly on the mean intensity $\bar{J} = \int J_\nu \phi_\nu d\nu$, their computation involves the knowledge of the absorption profile ϕ_ν. At low densities, such as those considered in this study, collisional broadening is negligible with respect to natural broadening, which defines the wings of the profile. The core is dominated by Doppler broadening, whose width is proportional to $(2kT/m + \xi^2)^{1/2}$ (where ξ is the microturbulent velocity; other symbols have their usual meaning). Whereas the thermal term $(2kT/m)$ is preponderant in the case of hydrogen lines, the microturbulent velocities observed in the solar chromosphere are too high to be neglected. As some correlation has been observed between ξ and T (cf. Feldman et al., 1978), we preferred, instead of neglecting ξ or introducing it as a new free parameter, to link the two quantities by the empirical formula:

$$\xi = 6 + 14\log(T/10^4) \quad (1)$$

which fits roughly the observations represented on the Fig. 4 of the paper by Feldman et al. Here, ξ is in km s^{-1} and T in kelvins.

2.1.3. Radiative bound-free rates

The radiative transition probabilities for hydrogen bound-free transitions depend on the radiation fluxes above the solar surface, in the corresponding frequency bandpasses. We defined these fluxes in terms of mean radiation temperatures: 6500 K, 5000 K and 4800 K for the Lyman, Balmer and Paschen continua, respectively.

2.1.4. Collisional rates

These rates follow from collisional cross-sections as functions of the energy of the incoming electron. As our computations cover a very large range of temperatures (almost 10^4 to 10^7 K), it was necessary, for Lα, to use cross sections from different sources:

(i) at low energies (10 to 11 eV), we used the experimental results of Williams and Willis (1974) for the $(1s - 2p)$ transition, and Koschieder et al. (1973) for $(1s - 2s)$;

(ii) at medium energies (11 to 50 eV), the cross-sections were taken from Mc Gowan et al. (1969);

(iii) at high energies ($\geq$ 50 eV), we used the formulae of Johnson (1972).

For other transitions, we used the compilation of Vernazza (1972).

2.1.5. Lyman-α source function

The source functions have been computed under two different assumptions with respect to photon scattering: complte redistribution (CR) and partial frequency redistribution (PFR). Although the second assumption is more realistic, the first one allows much faster computations, avoiding the lengthy calculation of redistribution functions. For PFR, we used a frequency-dependent coherence ratio, following Basri et al. (1979). The effect of anisotropic scattering is not studied here: since limb-darkening is very weak in Lα, and the emitting structure is lying at low altitude above the solar surface, the incoming radiation field is almost isotropic in a $2\pi\,sr$ solid angle. Thus, the light scattered horizontally will not depend on the angular redistribution function. In most of the Lα wavelength range, the continuous absorption coefficient is negligible with respect to that of the line, so that the source function calculation reduces to that of the line source function.

In the case of CR, it is possible, once the populations of atomic levels are obtained by solving the equations of statistical equilibrium, to compute the source function using the formula:

$$S = \frac{2h\nu^3}{c^2}\left(\frac{g_2}{g_1}\frac{N_1}{N_2} - 1\right)^{-1} \quad (2)$$

© European Southern Observatory • Provided by the NASA Astrophysics Data System

1986A&A...154..154G

However, for the sake of discussion, it is advantageous to distinguish between the contributions of scattering, collisional excitation and interlocking to the source function. Thus, following Jefferies (1968), we put S into the form:

$$S = \frac{\bar{J} + \varepsilon B_\nu(T) + \eta\tilde{B}}{1 + \varepsilon + \eta} \tag{3}$$

where η and $\eta\tilde{B}$ are combinations of all transition probabilities other than those corresponding to (1 – 2). To isolate the scattering term only, we reduce the expression of S to the more compact form:

$$S = \varepsilon^* B^* + (1 - \varepsilon^*)\bar{J} \tag{4}$$

Once obtained ε^* and B^*, it is also possible to calculate the source functions in the case of PFR, using the formula:

$$S_\nu = \varepsilon^* B^* + (1 - \varepsilon^*)\frac{1}{\phi_\nu}\int J_{\nu'} R_{\nu'\nu}\, d\nu' \tag{5}$$

The redistribution matrix was computed using a method analogous to that of Adams et al. (1971) but replacing, to save computer time, the spline representation of intensity by a piecewise representation. For the R_{II} function, we used a gaussian integration of the angle-dependent redistribution function when the two frequencies (for absorption and emission) lie within the line core, and the "wing" formula of Adams et al., otherwise.

2.1.6. Intensities

If Δl is the dimension of the object along the line of sight, the corresponding optical thickness at frequency ν will be:

$$\tau_\nu = \frac{h\nu_0}{4\pi} N_1 B_{12} \Delta l\, \phi_\nu \tag{6}$$

If the object is observed outside the solar disk, it will appear with the monochromatic intensity:

$$I_\nu = \int_0^{\tau_\nu(\Delta 1)} S_\nu e^{-t_\nu} dt_\nu = S_\nu(1 - e^{-\tau_\nu}) \tag{7}$$

For observations made over the disk, the intensity is:

$$I_\nu = I_\nu^0 e^{-\tau_\nu} + S_\nu(1 - e^{-\tau_\nu}) \tag{8}$$

(where I_ν^0 is the monochromatic intensity of the solar disk).

In both cases, we obtain the LRI by integrating I_ν over frequency and dividing the result by the mean disk intensity, as indicated above.

2.2. Results

We calculate here the intensities for pressures ranging from 10^{-2} to 10^2 dyn cm^{-2}, with a special emphasis on those lying between 0.1 and 10 dyn cm^{-2}, which correspond to most observed loops (cf.. Rosner et al., 1978). Pressures higher than 10 dyn cm^{-2} seem to occur only in flares, while those of order 10^{-2} dyn cm^{-2} might be associated with the cool cores of sunspot loops (Foukal, 1975, 1978).

2.2.1. Lyman-α emission mechanisms

Every process that populates atomic level 2 may be considered as an emission mechanism. These are the following (we write in parentheses the corresponding rates):

(i) Lα absorption ($N_1 B_{12}\bar{J}$)
(ii) collisional excitation from level 1 ($N_1 C_{12}$)
(iii) Hα emission ($N_3 A_{32}$)
(iv) collisional de-excitation from level 3 ($N_3 C_{32}$)
(v) radiative recombination in the Balmer continuum ($N_c R_{c2}$)
(vi) collisional recombination in the Balmer continuum ($N_c C_{c2}$).

The efficiencies of these processes are compared in Fig. 1a, as functions of pressure, for a typical temperature (10^5 K). It appears that:

– the collisional processes (iv) and (vi) are always negligible;
– the radiative rates (iii) and (v) associated with Hα and the Balmer continuum, respectively, have a variation with pressure nearly parallel to that of collisional excitation (ii), which dominates them by about an order of magnitude;
– the scattering of Lα radiation (i) dominates all processes for pressures lower than about 0.5 dyn cm^{-2}, but becomes less efficient than collisional excitation at higher pressures.

In Fig. 1b, we compare the two dominant processes (scattering and collisional excitation) by plotting the ratio $C_{12}/B_{12}\bar{J}$ as a function of temperature, for different values of the pressure (since this ratio is proportional to the electron density, and therefore to the pressure, all curves have the same shape). It appears that the variation of this ratio is nearly flat in a large range of temperature, with a maximum between 10^5 and $2\,10^5$ K. It decreases slowly towards high temperature, but sharply in the opposite direction, below 30000 K.

In brief, one may say that, in a large range of temperatures ($3\,10^4$ to 10^6 K), the dominant process is scattering at low pressures ($p \leq 0.5$ dyn cm^{-2}) and collisional excitation at higher pressures ($p \geq 1$ dyn cm^{-2}). This conclusion is not in contradiction with that of Gabriel et al. (1971) and Withbroe et al. (1982) (who said that collisional excitation was negligible) since these authors were both concerned with outer components of the solar corona, where densities are generally lower than those considered here.

2.2.2. Optical thickness

The line center optical thickness $\Delta\tau$ of the object along the line of sight is represented in Fig. 2 as a function of its pressure and temperature, for a given geometrical thickness $\Delta l = 1000$ km ($\Delta\tau$ is proportional to Δl). One may notice that, in the useful range of parameters, $\Delta\tau$ is essentially proportional to the pressure. Towards high temperatures, the relation $\log \Delta\tau = f(\log T)$ tends to be linear, and may be approximated by the simple relation:

$$\Delta\tau \sim P\,\Delta l\, 10^{-3.33-3.05x} \tag{9}$$

where P is expressed in dyn cm^{-2}, Δl in megameters and $x = \log(T/10^6\,\mathrm{K})$.

2.2.3. Intensities for objects observed outside the solar disk

In this case, the intensities may be computed from Eq. (7) and Eq. (4) or (5), depending on whether complete redistribution is assumed or not. The effect of the CR approximation on the profiles is illustrated in Fig. 3, where we consider 2 objects with different pressures and temperature. For the same set of physical parameters, the profiles computed in PFR and in CR are identical in the core, but the CR wing is higher than the PFR one. This difference disappears for high pressures, since collisional

© European Southern Observatory • Provided by the NASA Astrophysics Data System

1986A&A...154..154G

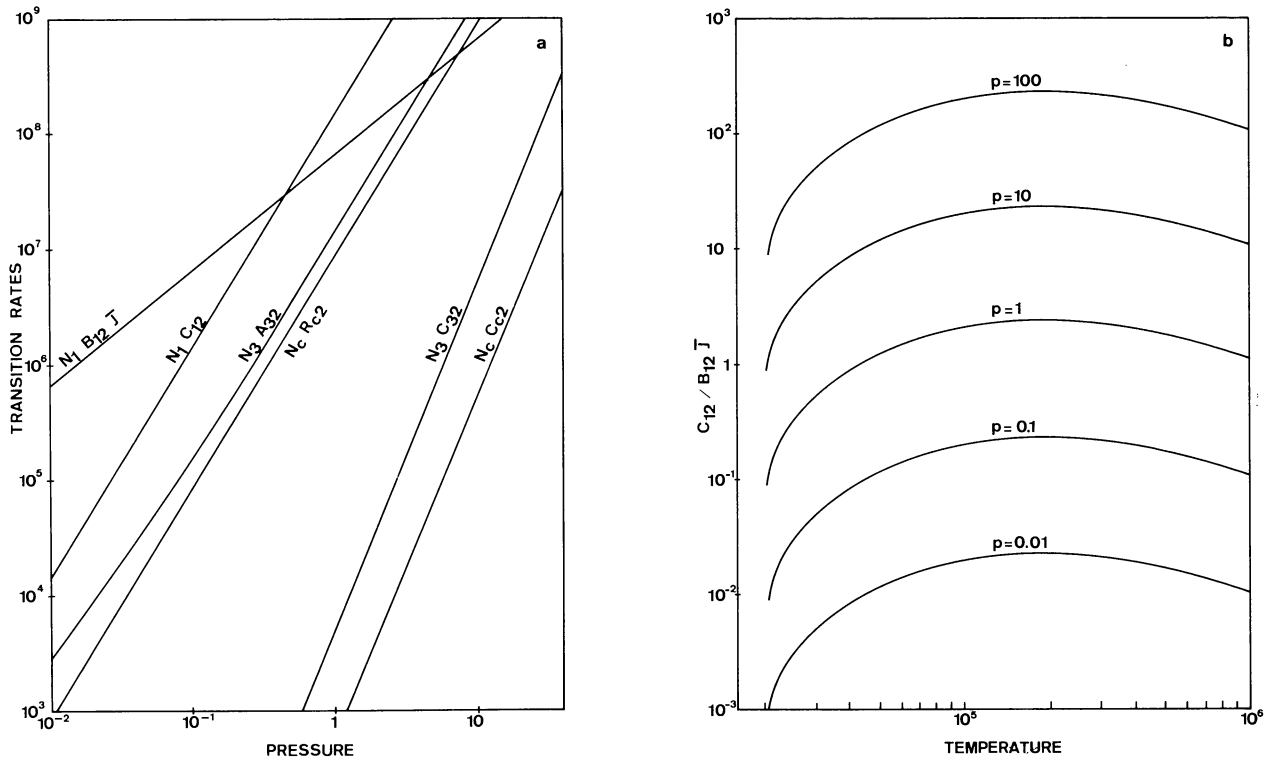

Fig. 1a and b. Comparison of efficiencies for different processes populating level 2 of the hydrogen atom. **a** Transition rates (in $cm^{-3}\,s^{-1}$) as functions of pressure (in dyn cm^{-2}) for a temperature of 10^5 K. The curves are labeled with the corresponding mathematical symbols. **b** Ratio or collisional to radiative excitation rates for the (1–2) transition, as a function of temperature (in kelvins) for different pressures, indicated (in dyn cm^{-2}) along the corresponding curves

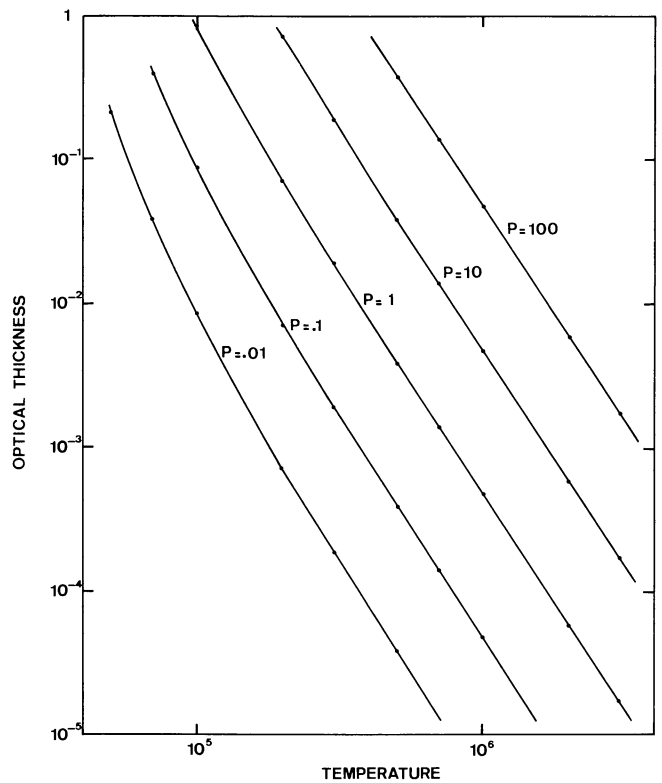

Fig. 2. Line center optical thickness as a function of temperature (in K) for different pressures (in dyn cm^{-2}, indicated along the curves), and a geometrical thickness of 1 Mm

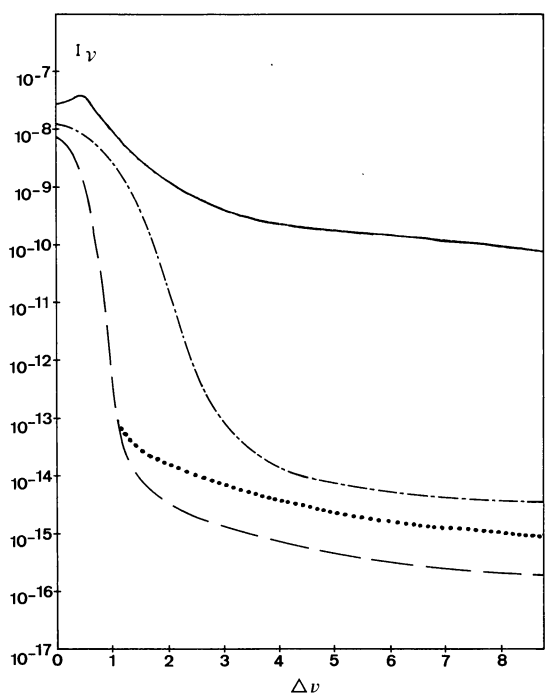

Fig. 3. Lyman-α monochromatic intensities (in erg $s^{-1}\,cm^{-2}\,sr^{-1}\,Hz^{-1}$) as a function of the distance to the line center measured in frequency units (THz). Solid line: solar disk intensities. Other lines: objects of 1 Mm thickness observed outside (and close to) the limb. Dashed line: pressure 0.1 dyn cm^{-2}, temperature 7 10^4 K, PFR. Dotted line: same object, but the intensities are calculated with the CR approximation. Dash-dotted line: pressure 10 dyn cm^{-2}, temperature 5 10^5 K (PFR and CR)

© European Southern Observatory • Provided by the NASA Astrophysics Data System

1986A&A...154..154G

excitation dominates scattering in this case. As the intensity in the wings is several orders of magnitude lower than that of the core, the difference between CR and PFR profiles has no consequence on the intensity integrated over frequency. Thus, the approximation of CR gives wrong profiles but good frequency-integrated intensities, for optically thin objects.

The corresponding LRI's are represented in Fig. 4a, as functions of pressure and temperature, for the same value of Δl (1 Mm) as above. Intensities like optical thicknesses, decrease rapidly with temperature. Here, the curves are unequally spaced in logarithmic scales: towards low pressures, where scattering dominates, the LRI varies linearly with the optical thickness, and thus with the pressure. On the other hand, at high pressures, the emission is dominated by collisional excitation and varies as the product $N_e \times N_1$, i.e. as the square of the pressure (one may check that the two lower curves are separated by about one order of magnitude, while the two upper ones are separated by two orders). In fact, as other processes populating level 2 are not really negligible, it is not possible to give an empirical formula both precise and simple for the LRI. Nevertheless, we may obtain an estimate of the LRI using a formula with a linear and a quadratic term in P:

$$\mathrm{LRI} \approx \Delta l \left[1.3 \times 10^{-4} \left(\frac{T}{10^6} \right)^{-3} P + 2.1 \times 10^{-4} \left(\frac{T}{10^6} \right)^{-3.5} P^2 \right] \quad (10)$$

where Δl is in megameters, T in kelvins and P in dyn cm^{-2}.

2.2.4. Intensities for objects observed on the disk

Using Eq. (8), we can obtain the LRI for a structure observed on the disk, as a function of its pressure and temperature. The result is represented in Fig. 4b, for a geometrical thickness of 1 Mm. As the temperature increases, the optical thickness tends to zero, and the LRI to 1. Towards low temperatures, the variation of constrast vs. temperature is very different depending upon the value of the pressure: below a transition value (about 0.4 dyn cm^{-2}) the structure appears darker than the surrounding solar disk, while, for higher pressures, it is brighter. The reason of this may be easily understood from Sect. 2.2.1: in the scattering process, radiation absorbed in a 2π *sr* solid angle is reemitted into 4π *sr*, and thus diluted. On the contrary, collisional excitation produces a reinforcement of the Lα intensity without absorption of photons from the solar disk.

As the pressure controls the ratio between collisional excitation and scattering, it determines also the observed intensity of the structures. Thus, *the contrast of structures observed on the solar disk in Lα constitutes a diagnostic of pressure rather than temperature.*

Towards low intensities, it should be noticed that LRI lower than 0.9 cannot be produced by optically thin structures. Thus, the dark loops observed by Bonnet and Tsiropoula (1982) are probably low-temperature, optically thick objects, as is shown below.

3. Optically thick slabs

When temperature decreases, coronal loops become optically thick in Lα, and successively in other Lyman lines, Lyman continuum, Balmer lines, etc. Then, radiative transfer equations must be solved for all relevant transitions, together with the steady state equations for pressure, ionization and atomic level populations.

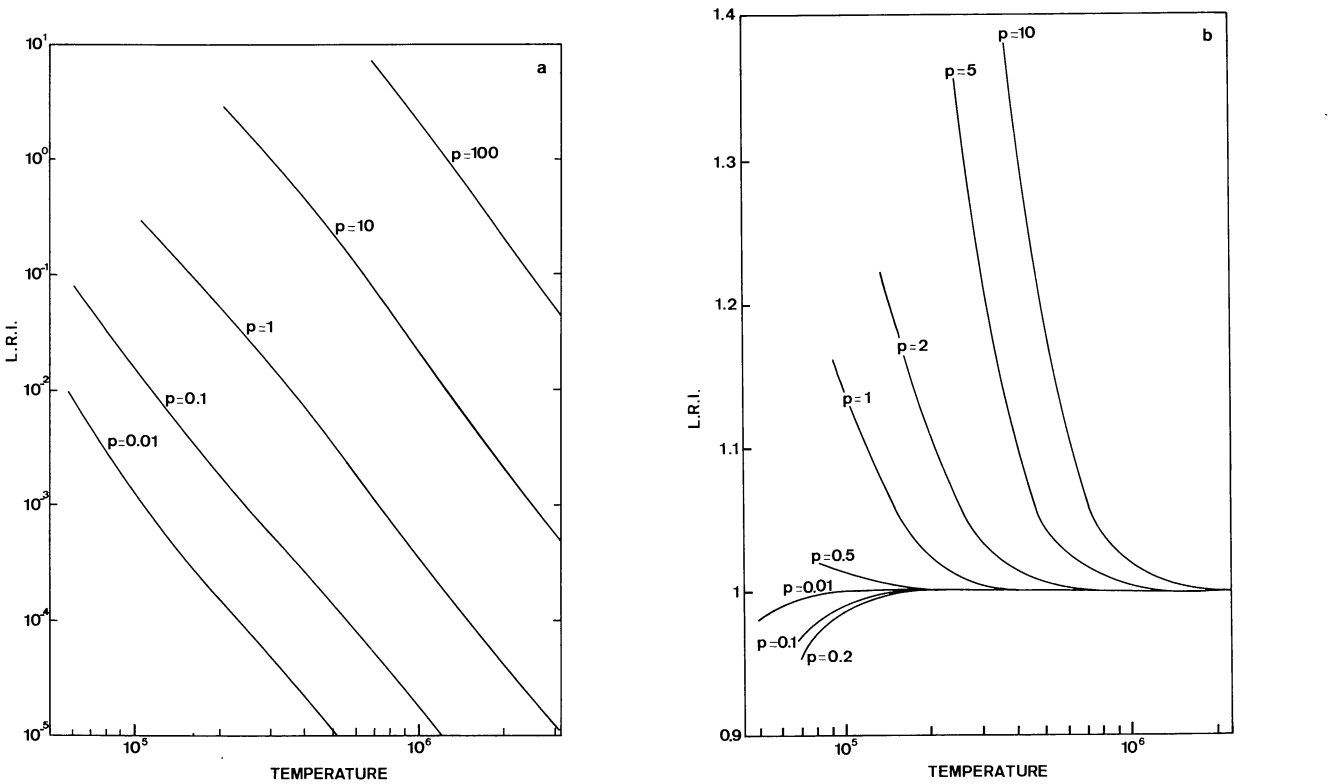

Fig. 4a and b. Optically thin objects: relative frequency-integrated intensities as functions of temperature (K) for a geometrical thickness of 1 Mm. **a** observations out of the limb, **b** observations on the disk. Each curve corresponds to a constant pressure, which is indicated in dyn cm^{-2}

© European Southern Observatory • Provided by the NASA Astrophysics Data System

1986A&A...154..154G

To solve the radiative transfer equations numerically, we must assume that the object has a simple geometry, so that, in this section, we shall limit ourselves to the study of plane-parallel slabs, either vertical or horizontal with respect to the solar surface. In each case, the slab will be assumed perpendicular to the direction of the observer, so that results obtained in the horizontal case can be used for comparison with objects observed near the center of the solar disk, while the vertical case can be associated with observations at the limb.

3.1. Computational methods

The equilibrium equations for atomic level populations, electron density and pressure are solved iteratively. Between two successive iterations on these state variables, a number of iterations is performed on radiation fields in lines and bound-free continua. For each of these transitions, an equivalent two-level atom approach is used, and the intensities and source functions are computed by the Feautrier method. These iterations proceed until all convergence criteria (on electron density, level population and radiation fields) are statisfied. Adjustable relaxation parameters are used in order to optimize the convergence properties of the system.

Most computations assume a three-level plus continuum hydrogen atom, similar to that described in the preceding section. The standard assumptions in the treatment of photon scattering are PFR for the Lα and Lβ lines, and CR for Hα. For the sake of comparison, some other computations are done using the CR assumption for all lines, which is less realistic, but often used in the literature. In order to evaluate the influence of the limitation in the number of atomic levels, some models have been recomputed with a 5 level plus continuum hydrogen atom, with a PFR treatment of Lα and Lβ and a CR one for the 8 other lines.

For a horizontal slab, the lower boundary condition is defined by the incident intensities in lines and continua, which are equal to those emitted by the solar disk, while the upper boundary condition corresponds to zero incident intensities. For a vertical slab, we use the same intensities, divided by 2, incident on both sides (in this last case, computations are done with one half-slab only, taking advantage of the symmetry). In 3 level plus continuum computations, the intensities emitted by the solar disk are 2 times the mean intensities used in the optically thin case of the preceding section. When using a 5 level plus continuum atom, we complement this intensity set in the following way: Lγ and Lδ are assumed to have the same profiles as Lβ, but the intensities are scaled by the ratio of frequency-integrated intensities measured by Vernazza and Reeves (1978). For the Hβ and Hγ lines, we used line profiles by David (1961). For the Pα, Pβ and Bα lines, which are less important for statistical equilibrium population of level 2, we simply used the continuum values of incident radiations. For bound-free transitions from level 4 and 5, we used mean radiation temperatures of 4550 and 4300 K, respectively.

The emergent intensities are computed from optical depths and source functions, using formulae similar to (8) or (7), according as the slab is horizontal or vertical (in this last case, we first reconstruct the symmetric, full slab from the half-slab used in the computations).

3.2. Results

The computations done for plane-parallel slabs are summarized in Table 1. In order to keep the total amount of computing time within reasonable limits, we restrict our investigation to 1 significant geometrical depth (1 Mm) and 4 pressures (0.01, 0.1, 1 and 10 dyn cm^{-2}). In every case, the computations are done for both horizontal and vertical slabs. The range of temperatures considered depends on the pressure and corresponds approximately to the useful range of optically thick slabs. For $p = 10$ dyn cm^{-2}, this interval is limited to 10^5 and $2\,10^5$ K, since lower temperatures give too high, unrealistic intensities. Computations done, for comparison, with a 5-level plus continuum atom or with the CR approximation, are restricted to $p = 0.1$ dyn cm^{-2}. As results of these computations, we give in Table 1 the optical thickness of the slab at the center of the Lyman-α line, which is an indicator of the mean ionization of hydrogen, and the LRI.

3.2.1. Horizontal slabs

The variations of frequency-integrated intensities vs. temperature are represented, for horizontal slabs, in Fig. 5. These variations are strongly dependent on pressure. For high pressure loops (1 dyn cm^{-2}), which are collision-dominated as seen in the preceding section, the decrease of temperature from about $2\,10^5$ K

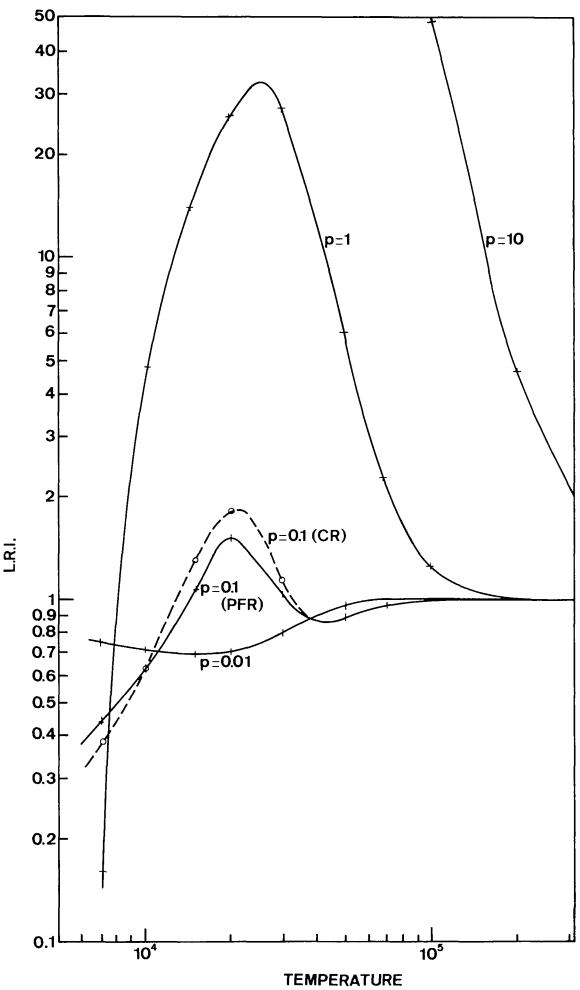

Fig. 5. Relative frequency-integrated intensities for horizontal plane-parallel slabs of thickness 1 Mm, as functions of temperature. Each curve corresponds to a constant pressure, which is indicated in dyn cm^{-2}. Solid curves refer to PFR computations in the Lyman lines. The dashed curve corresponds to the CR approximation

© European Southern Observatory • Provided by the NASA Astrophysics Data System

1986A&A...154..154G

Table 1. Summary of computations for plane-parallel slabs

Pressure (dyn cm^{-2})	Temperature (K)	Position (H=horiz. V=vertical)	Number of discrete levels	Redistribution (P = partial C = complete)	Optical depth at line center	Relative intensity (LRI)
0.01	7000	H	3	P	4.05 (+3)	7.47 (-1)
0.01	7000	V	3	P	4.04 (+3)	1.45 (-1)
0.01	10000	H	3	P	1.19 (+3)	7.21 (-1)
0.01	10000	V	3	P	1.17 (+3)	1.59 (-1)
0.01	15000	H	3	P	2.95 (+2)	6.96 (-1)
0.01	15000	V	3	P	2.95 (+2)	1.86 (-1)
0.01	20000	H	3	P	9.12 (+1)	6.97 (-1)
0.01	20000	V	3	P	9.13 (+1)	2.00 (-1)
0.01	30000	H	3	P	6.44	8.01 (-1)
0.01	30000	V	3	P	6.44	1.59 (-1)
0.01	50000	H	3	P	2.15 (-1)	9.68 (-1)
0.01	50000	V	3	P	2.15 (-1)	2.35 (-2)
0.1	7000	H	3	P	2.21 (+5)	4.43 (-1)
0.1	7000	H	3	C	3.01 (+5)	3.77 (-1)
0.1	7000	V	3	P	2.17 (+5)	3.72 (-1)
0.1	7000	V	3	C	2.94 (+5)	3.41 (-1)
0.1	10000	H	3	P	5.15 (+4)	6.27 (-1)
0.1	10000	H	3	C	7.97 (+4)	6.32 (-1)
0.1	10000	H	5	P	5.76 (+4)	6.27 (-1)
0.1	10000	V	3	P	5.17 (+4)	3.54 (-1)
0.1	10000	V	3	C	7.92 (+4)	4.15 (-1)
0.1	10000	V	5	P	5.78 (+4)	3.73 (-1)
0.1	15000	H	3	P	6.06 (+3)	1.10
0.1	15000	H	3	C	6.06 (+3)	1.30
0.1	15000	V	3	P	6.15 (+3)	7.54 (-1)
0.1	15000	V	3	C	6.14 (+3)	9.57 (-1)
0.1	20000	H	3	P	1.41 (+3)	1.50
0.1	20000	H	3	C	1.30 (+3)	1.80
0.1	20000	H	5	P	1.44 (+3)	1.55
0.1	20000	V	3	P	1.43 (+3)	1.17
0.1	20000	V	3	C	1.31 (+3)	1.46
0.1	20000	V	5	P	1.46 (+3)	1.22
0.1	30000	H	3	P	7.58 (+1)	1.04
0.1	30000	H	3	C	7.55 (+1)	1.12
0.1	30000	V	3	P	7.58 (+1)	6.47 (-1)
0.1	30000	V	3	C	7.56 (+1)	7.21 (-1)
0.1	50000	H	3	P	2.22	8.90 (-1)
0.1	50000	H	3	C	2.22	8.90 (-1)
0.1	50000	H	5	P	2.38	8.89 (-1)
0.1	50000	V	3	P	2.22	1.83 (-1)
0.1	50000	V	3	C	2.22	1.83 (-1)
0.1	50000	V	5	P	2.38	1.94 (-1)
0.1	70000	H	3	P	3.92 (-1)	9.56 (-1)
0.1	70000	V	3	P	3.92 (-1)	5.79 (-2)
1	7000	H	3	P	4.33 (+6)	1.60 (-1)
1	7000	V	3	P	4.30 (+6)	5.32 (-1)

© European Southern Observatory • Provided by the NASA Astrophysics Data System

1986A&A...154..154G

Table 1 (continued)

Pressure (dyn cm^{-2})	Temperature (K)	Position (H=horiz. V=vertical)	Number of discrete levels	Redistribution (P = partial C = complete)	Optical depth at line center	Relative intensity (LRI)
1	10000	H	3	P	2.99 (+5)	4.77
1	10000	V	3	P	3.03 (+5)	4.77
1	15000	H	3	P	1.82 (+4)	1.39 (+1)
1	15000	V	3	P	1.86 (+4)	1.35 (+1)
1	20000	H	3	P	4.62 (+3)	2.68 (+1)
1	20000	V	3	P	4.70 (+3)	2.63 (+1)
1	30000	H	3	P	5.76 (+2)	2.71 (+1)
1	30000	V	3	P	6.02 (+2)	2.70 (+1)
1	50000	H	3	P	2.21 (+1)	5.99
1	50000	V	3	P	2.21 (+1)	5.45
1	70000	H	3	P	3.92	2.27
1	70000	V	3	P	3.92	1.67
1	100000	H	3	P	8.61 (-1)	1.25
1	100000	V	3	P	8.61 (-1)	4.70 (-1)
10	100000	H	3	P	8.55	5.04 (+1)
10	100000	V	3	P	8.55	4.82 (+1)
10	200000	H	3	P	6.89 (-1)	4.59
10	200000	V	3	P	6.89 (-1)	3.77

first causes an increase of intensity, as the slab becomes more and more optically thick. This process is balanced by the decrease of excitation so that a maximum is reached between $3\,10^4$ and $2\,10^4$ K. At low temperatures, the slab becomes very opaque and the emitted intensity drops sharply, as the Planck function.

For a lower pressure (0.1 dyn cm^{-2}), the variation is more complex. As temperature decreases, the appearance of opacity first causes a decrease in intensities since, as seen for optically thin objects, the radiation absorbed within 2π steradians is scattered into 4π. But, below $4\,10^4$ K, the intensity begins to increase, as a result of the imprisonment of Lα radiation within the slab which produces a higher mean excitation (this effect was not predictable from optically thin analysis). A maximum is reached near $2\,10^4$ K and, below this temperature, the intensity decreases as in the preceding case.

For very low pressures (0.01 dyn cm^{-2}), the intensity decreases regularly as the slab becomes cooler, from 10^5 to $2\,10^4$ K. At lower temperatures, it rises slowly again. This effect may be understood from Fig. 6: as the temperature decreases, the absorption feature, at the center of the line, becomes both deeper (as optical thickness increases) and narrower (as Doppler width decreases). When the central intensity comes close to zero, the increase of transmission due to the decrease of absorption width becomes more important than the increase of absorption at line center. Thus, for a low-pressure low-temperature structure observed on the disk, the contrast on Lα filtergrams may be weak, whereas the optical thickness at line center is high. This might explain why some

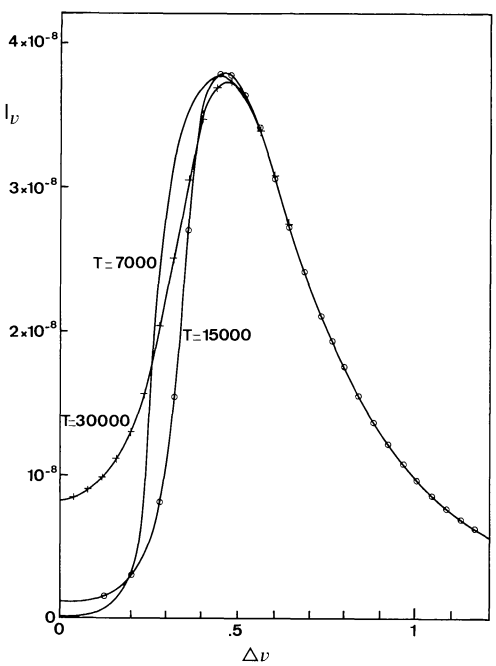

Fig. 6. Lyman-α line profiles for horizontal slabs of thickness 1 Mm and pressure 0.01 dyn cm^{-2}, observed at normal incidence. Each curve corresponds to a given temperature, indicated in K. Frequencies are in THz and intensities in erg s^{-1} cm^{-2} sr^{-1} Hz^{-1}

© European Southern Observatory • Provided by the NASA Astrophysics Data System

1986A&A...154..154G

filaments appear with higher contrast in Hα pictures than in Lα pictures (cf. Bonnet et al., 1980), whereas the optical thickness in the former line is certainly much smaller than in the latter.

3.2.2. Vertical slabs

Figure 7 is similar to Fig. 5, but concerns vertically standing slabs observed outside (but close to) the solar limb. High pressure (10 and 1 dyn cm^{-2}) vertical slabs emit about the same intensities as the corresponding horizontal slabs, since the main part of emission comes from collisional excitation inside the slab itself. The curves differ at both ends: towards high temperature, we find again the optically thin case, where LRI goes to 0 for vertical slabs instead of 1 for horizontal slabs. Towards low temperatures, whereas the LRI's for horizontal slabs decrease rapidly, those corresponding to vertical slabs seem to stabilize near 0.5. As we have only one computed point in this region (LRI = 0.53 for $p = 1$ dyn cm^{-2}, $T = 7000$ K), we cannot be very affirmative concerning this asymptotic behaviour but, if true, it may find the following explanation: at low temperatures, collisional excitation becomes negligible so that the emission of the slab is formed principally by radiation from the solar disk which is scattered back. Since the optical thickness is very large, and the photon destruction probability small enough, the albedo of the slab is close to 1. The value 0.5 comes from the dilution of radiation into an emission solid angle 2 times larger than that of absorption (cf. Vial, 1982).

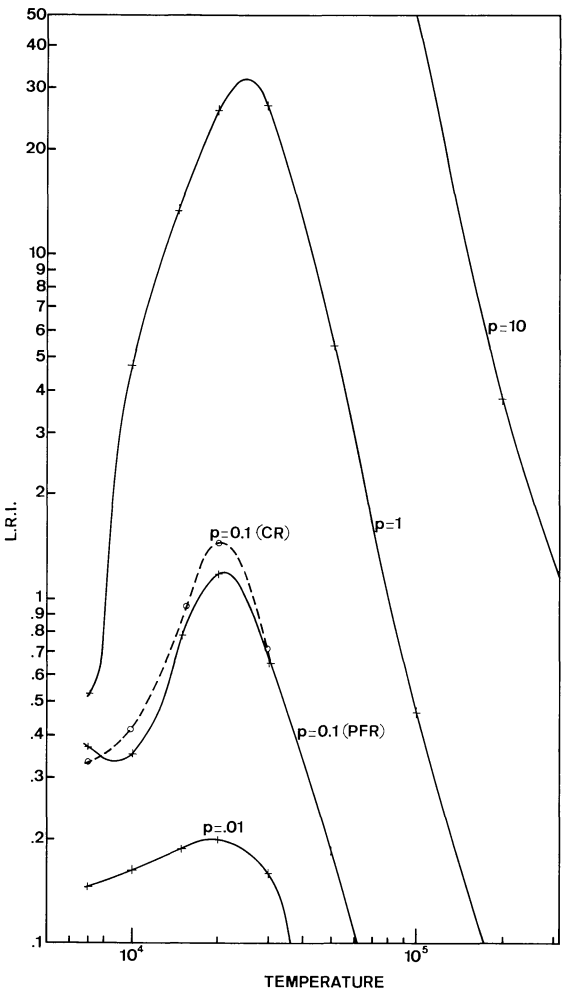

Fig. 7. Same as Fig. 5, but for vertical slabs

For a lower pressure (0.1 dyn cm^{-2}), there is also some similarity between the curves corresponding to vertical and horizontal slabs, since both curves have a maximum near $T = 20000$ K. But the intensities emitted by the vertical slab are, in this case, significantly smaller than those emitted by the horizontal one. The difference may be roughly explained remarking that the intensity emitted by the vertical slab is due to photons emitted in the slab itself. For the corresponding horizontal slab, the internal emission is not very different (provided that the optical thickness is not too large), but we must add to the intensity the contribution of photons from the solar disk that go through the slab without being absorbed, especially in the wings of the absorption profile. Towards low temperatures, the situation tends to be reversed as the optical depth grows: thermalization becomes effective and the brightness of the vertical slab grows again towards 0.5, while that of the horizontal one continues to decrease, as in the high pressure case.

In the very low pressure case (0.01 dyn cm^{-2}), the slab remains optically thin for the main part of the photons emitted by the sun, so that the LRI is low: the maximum, near 0.2, is reached around $T = 20000$ K. Towards high temperatures, the sharp decrease of intensity is due to that of optical thickness. Towards low temperatures, we observe a slower decrease related to that of the Doppler width of the absorption profile in such a way that, whereas the optical thickness at line center continues to grow, the fraction of solar photons intercepted by the slab decreases (this is the same process that explains the increase of intensity of the corresponding horizontal slab).

3.2.3. Partial or complete redistribution?

In order to evaluate the validity of the CR approximation, we made another series of computations (restricted to $p = 0.1$ dyn cm^{-2}) with this assumption. The consequences on LRI result from 3 different effects:

(i) CR increases the intensities in the line wings. This effect is a general property of noncoherent scattering, and applies also to the solar chromosphere, stars. etc . . . It tends to increase the integrated intensity, for horizontal as for vertical slabs.

(ii) CR reduces the excitation in the central part of the slab. As pointed out by Heinzel (1984), the coherency of scattering in the wings of the absorption profile makes easier the penetration of Lα radiation into the central part of the slab, thus increasing level 2 population and source function. This effect tends to increase PFR source functions and intensities with reference to CR ones. It is particularly important for cool and thick slabs.

(iii) CR reduces the ionization in the central part of the slab, and consequently increases the optical thickness. It is a consequence to the preceding effect: since level 2 is less populated inside the slab, photoionization by the Balmer continuum is less efficient, so that the density of neutral hydrogen is increased. This effect tends to decrease the LRI of horizontal slabs and to increase that of vertical ones (as the preceding one, it is particularly efficient at low temperatures).

The global result is that, for vertical slabs, CR intensities are generally higher than PFR ones, except for the lowest temperature (7000 K). For horizontal slabs, CR intensities are lower at low temperatures (7000 K), and higher at medium temperatures

© European Southern Observatory • Provided by the NASA Astrophysics Data System

1986A&A...154..154G

(20000 K). At high temperatures (optically thin case), the difference is negligible, as shown in Sect. 2. The maximum departure, for the case under study ($\Delta l = 1$ Mm, $p = 0.1$ dyn cm^{-2}) is about 30%.

It should be noticed that, among the above mentioned effects of redistribution, the third one (concerning ionization) requires a self-consistent treatment of statistical and ionization equilibria, and radiative transfer with the appropriate redistribution functions. Thus, the procedure (sometimes used) of treating equilibrium equations with CR radiative transfer and using PFR in the final computation of Lα profiles only, is not satisfactory.

3.2.4. 3 or 5 levels?

We also made a series of computations using a 5 level plus continuum hydrogen atom, in order to evaluate the consequences of the reduction of the number of atomic levels. This series was also restricted to $p = 0.1$ dyn cm^{-2}. The results, given in Table 1, show that the intensities obtained with 5 levels are always greater than (or equal to) those computed with 3 levels, since cascades tend to increase the population of level 2, but that the difference is small: for the present series of computations, relative departures are all lower than 6% (the difference may be more important for Hα).

We may thus conclude that a 3-level plus continuum atom is in general a sufficient approximation for the computation of Lα intensities.

4. Optically thick cylinders

The plane-parallel geometry, assumed in the computations of the preceding section, had the advantage of using one-dimensional radiative transfer routines, which are relatively reliable and fast, thus allowing their repeated use within logical loops including a number of other equations (ionization, statistical equilibrium, etc.). But, as long as solar coronal loops are concerned, a cylindrical geometry is much more realistic. From the point of view of radiative transfer, the study of such objects requires not only the use of cylindrical coordinates, but also a full 2-dimensional treatment, since the incident radiation field is not symmetrical with respect to the axis of the cylinder (except in the special case where this axis is vertical). At the present time, there does not exist any fast and reliable method, using either difference-equation or integral-equation methods, to solve this problem, so that we turn towards a Monte-Carlo method, with an equivalent two-level atom. This approach has some limitations, especially in the range of optical thicknesses that can be treated correctly, but the comparison with plane-parallel calculations may help to construct some reliable extrapolations.

4.1. Method

The Monte-Carlo method considered here consists in a simulation of the random walk of Lα photons through the cylinder, following the general principles described, for instance, by Cashwell and Everett (1959). The case of photons in cylindrical geometry has been treated by several authors, in particular Avery et al. (1969).

In practice, such a method is limited to a 2-level atom, so that we first computed the net result of all other transitions of the 3-level plus continuum hydrogen atom on the Lα line, in the optically thin approximation. This result consists in two parameters:

(i) a "creation ratio" (η) which is the ratio of the number of atoms that come to level 2 by different processes (except Lα absorption) to those which are excited by Lα absorption, in the same volume and during the same time.

(ii) a "destruction probability" (ε), which represents the fraction of atoms in level 2 that leaves this level by another process than emission of a Lα photon.

The validity of this method is restricted to moderate optical thicknesses in Lα. The principal reason is that it assumes that the ionization equilibrium, which determines the opacities, is approximately uniform. Since this equilibrium depends principally on bound-free continua, one may expect that the preceding condition is satisfied when these continua are optically thin. For the range of temperatures considered here, the ratio between the optical thicknesses at the center of Lα and the head of the Lyman continuum is greater than 10^3, while the opacities in the Balmer and higher continua are still lower than that of the Lyman continuum. Thus, we decided to restrict the present computations to optical thicknesses lower than 10^3 at the center of Lα and to check the approximate uniformity of ionization with the multilevel computations of the preceding section. Another reason to limit the optical thicknesses of our cylinders is that, in the Monte-Carlo method, the computer time grows (approximately linearly) with the mean number of scatterings per photon and thus with the optical thickness.

Finally, it may be expected that the effects of curvature, which constitute the important part of the difference between the cylindrical and plane-parallel cases, become less and less important as the optical thickness increases, so that the case of moderately thick cylinders is probably the most interesting to study.

The principle of the calculation is summarized in Fig. 8. We consider two different sources of primary photons: emission by the solar disk and internal creation by electron collisions and other processes, expect Lα absorption, that populate level 2. The relative contributions of these two sources are determined by the creation ratio η, arising from optically thin statistical equilibrium. Some photons emitted by the disk go through the cylinder without absorption. Some photons created in the cylinder escape directly. The others undergo a number of scatterings, where they have the probability ε to be destroyed. The photons escaping from the cylinder, with or without scatterings, are recorded by different counters. Directional counters record the polar coordinates (θ, ϕ) of the direction of escape. We also define two exit "windows": an upper window ($\theta \leq 30°$) simulates observations near the center of the solar disk, while a side window ($60° \leq \theta \leq 120°$, $-30° \leq \phi \leq 30°$) represents observations near the limb, perpendicularly to the axis of the cylinder. When a photon escapes by one of these windows, special counters record their frequency, in order to have the line profile, and the distance of their trajectory to the axis of the cylinder, to obtain the tranverse variation of intensity. In addition, some similar counters record the primary photons emitted by the disk, which give the reference flux for the calculation of the LRI.

4.2. Results

We performed computations for 9 models of cylinders with a diameter of 1 Mm and different values for pressure and temperature. In every case, the axis of the cylinder was horizontal. These computations are summarized in Table 2, which contains, in ad-

© European Southern Observatory • Provided by the NASA Astrophysics Data System

1986A&A...154..154G

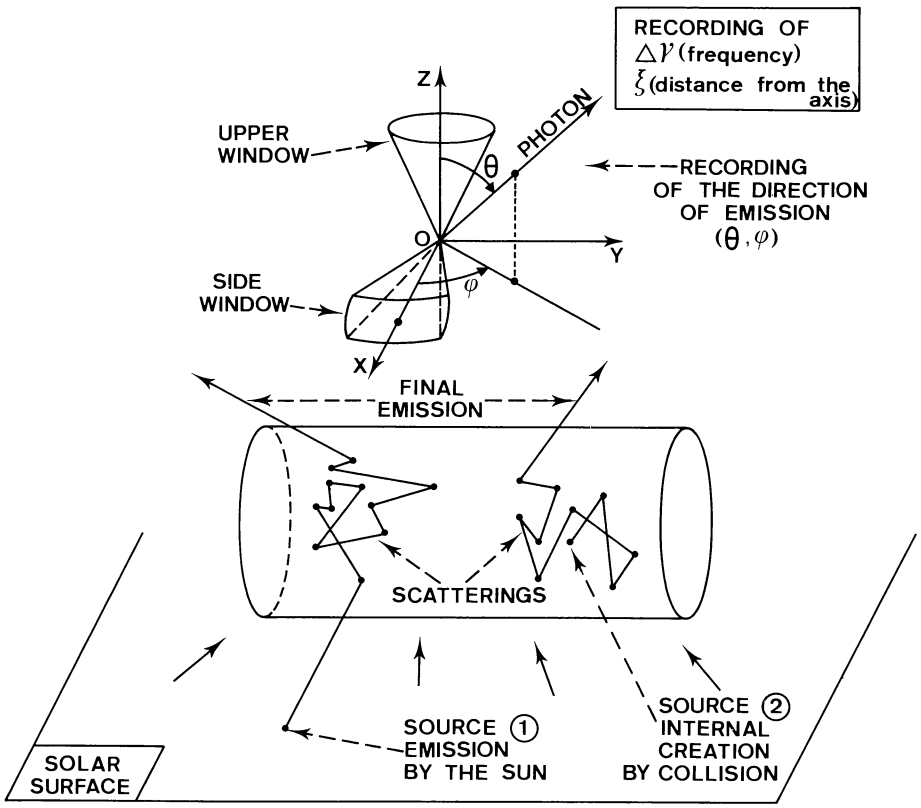

Fig. 8. Illustration of the Monte-Carlo method used for the computation of radiative transfer in cylindrical objects

Table 2. Summary of computations for cylinders

Pressure (dyn cm^{-2})	Temperature (K)	Micro-turbulence (km s^{-1})	Optical thickness at line center	Creation ratio	Destruction probability	LRI for upper window	LRI for side window
0.01	20000	10.2	9.79 (+1)	2.53 (−3)	6.64 (−4)	7.12 (−1)	2.33 (−1)
0.01	30000	12.7	6.55	6.13 (−3)	7.71 (−4)	8.19 (−1)	1.63 (−1)
0.01	50000	15.8	2.16 (−1)	1.45 (−2)	9.22 (−4)	9.78 (−1)	2.26 (−2)
0.1	30000	12.7	7.87 (+1)	4.66 (−2)	7.83 (−4)	9.76 (−1)	6.27 (−1)
0.1	50000	15.8	2.22	1.30 (−1)	9.32 (−4)	8.91 (−1)	1.70 (−1)
0.1	70000	17.8	3.92 (−1)	1.97 (−1)	1.03 (−3)	9.64 (−1)	5.67 (−2)
1	50000	15.8	2.23 (+1)	1.29	1.03 (−3)	4.40	4.03
1	70000	17.8	3.92	1.95	1.11 (−3)	1.91	1.37
1	100000	20.0	8.69 (−1)	2.49	1.19 (−3)	1.26	4.80 (−1)

dition to the fundamental variables (pressure and temperature), the following data:

– the microturbulent velocity, assumed to be related to temperature by Eq. (1)

– the optical thickness along a diameter, computed at the center of the Lα line

– the creation ratio η and the destruction probability ε, computed from statistical equilibrium, as explained above,

and, as results of the computations:

– the relative intensities, measured close to the axis of the cylinder, for both exit windows. The LRI corresponding to upper and lateral windows are to be compared to those emitted by horizontal and vertical slabs, respectively.

4.2.1. Line profiles

An advantage of the Monte-Carlo method is to give a direct insight into the process of line formation, by recording photons from different origins in different counters. The results of this procedure are represented in Fig. 9, for three different loop models. The first one is a low-pressure (0.1 dyn cm^{-2}), optically thick ($\tau \sim 80$) loop. The second one has the same pressure, but the

© European Southern Observatory • Provided by the NASA Astrophysics Data System

1986A&A...154..154G

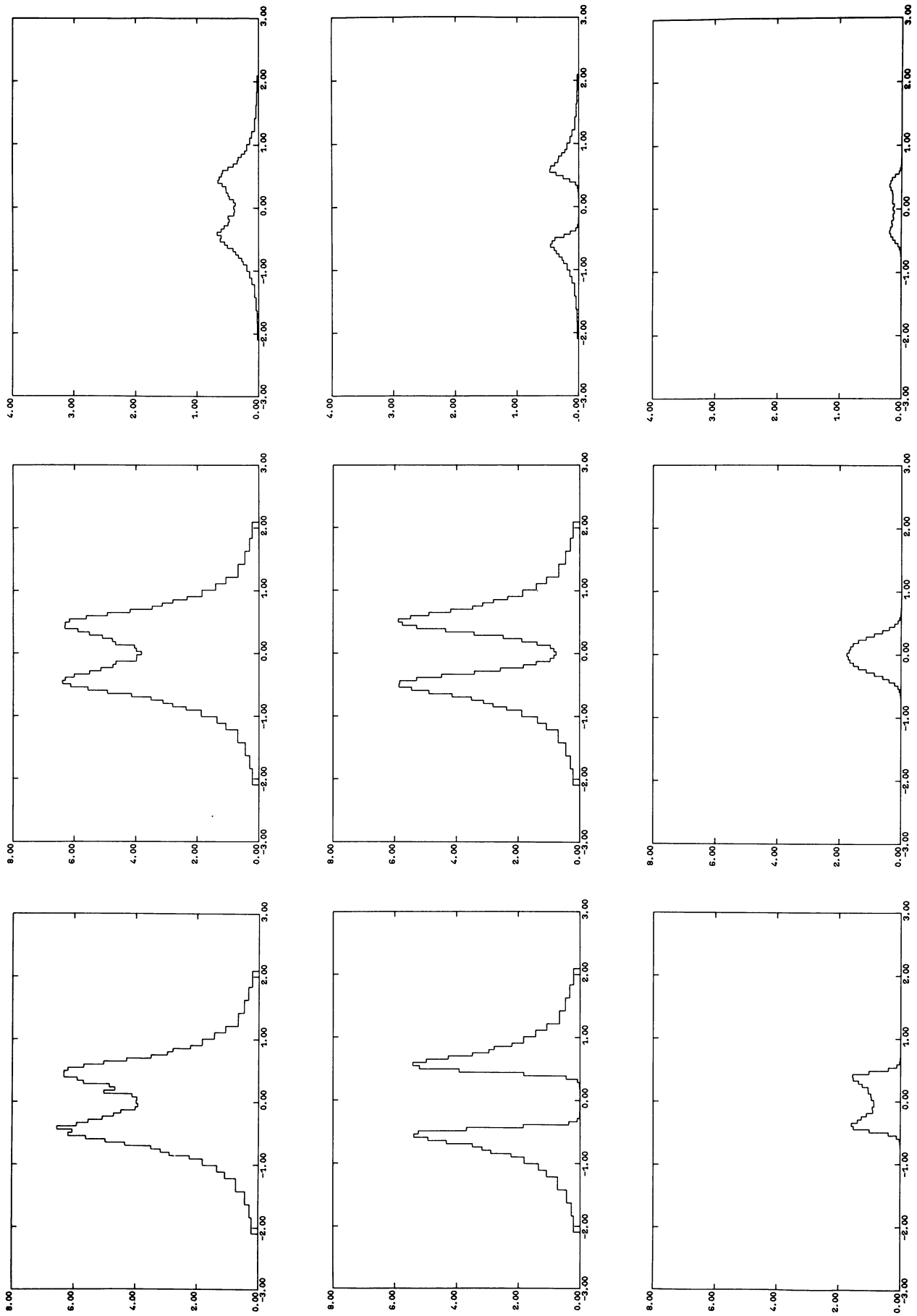

© European Southern Observatory • Provided by the NASA Astrophysics Data System

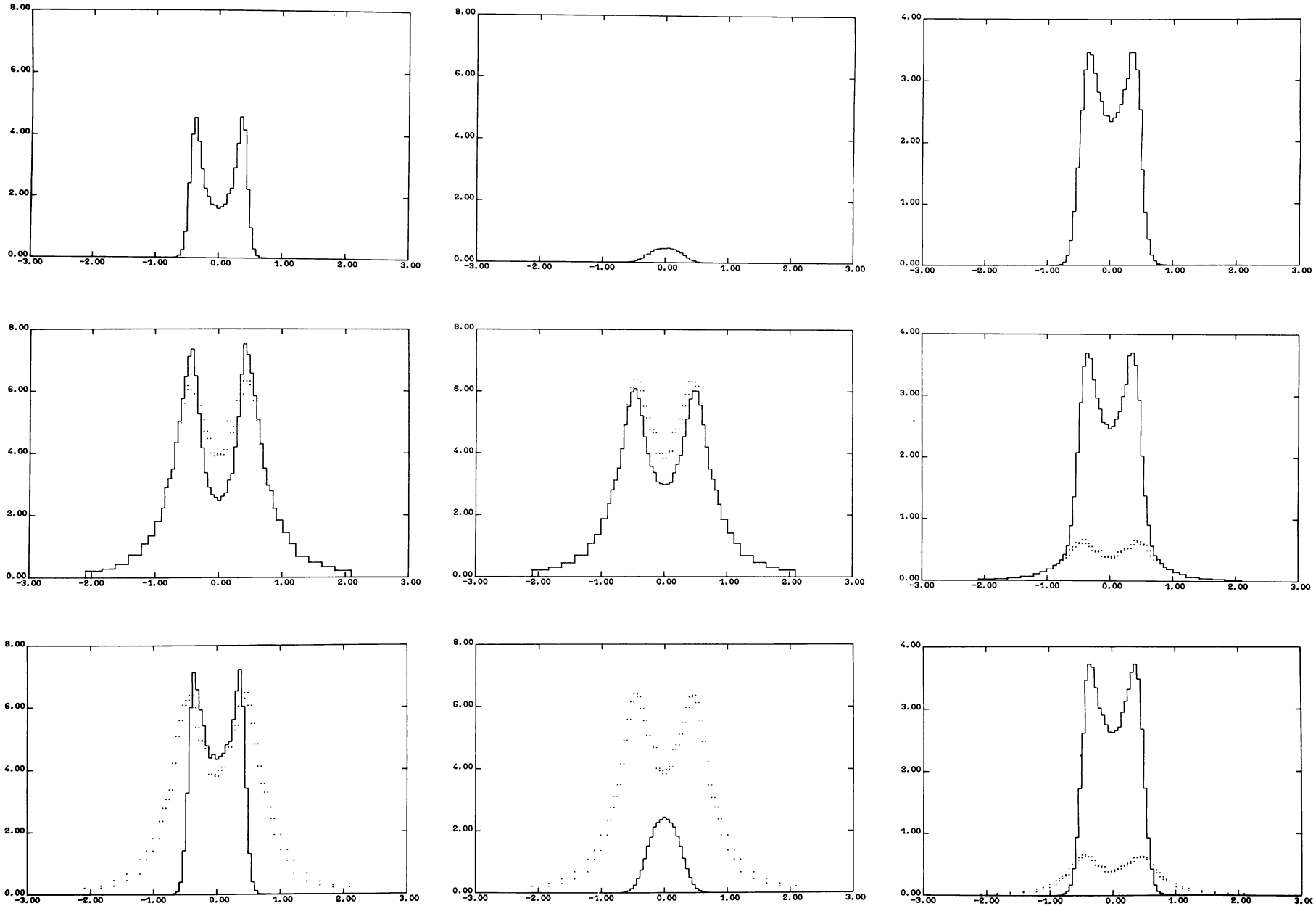

Fig. 9. Line formation in cylindrical objects. From top to bottom: *1st row:* profiles emitted by the solar disk. *2nd row:* profiles for photons crossing the cylinder without absorption *3rd row:* profiles for photons coming from the solar disk and subsequently scattered. *4th row:* profiles for photons created in the cylinder. *5th row:* resulting profiles (sums of 2nd, 3rd and 4th rows). The reference solar disk profile is indicated by a dotted line. The 5 first rows correspond to observations through the upper window. The *6th row* is the same as the *5th*, but for observations by the side window. Each column corresponds to a different model. From left to right: (i) $p = 0.1\,\mathrm{dyn\,cm^{-2}}$, $T = 30000\,\mathrm{K}$. (ii) $p = 0.1\,\mathrm{dyn\,cm^{-2}}$, $T = 50000\,\mathrm{K}$. (iii) $p = 1\,\mathrm{dyn\,cm^{-2}}$, $T = 50000\,\mathrm{K}$. Frequencies are in THz. The intensity scales are arbitrary, but constant within each column.

© European Southern Observatory • Provided by the NASA Astrophysics Data System

1986A&A...154..154G

temperature is higher, so that it is close to the optically thin case ($\tau \sim 2$). The third model is again an optically thick one ($\tau \sim 20$) but the pressure is higher (1 dyn cm^{-2}). The line profiles of incident radiation from the solar disk are, of course, the same in the three cases. The differences that can be observed on the figure are due to the statistical noise pertaining to the Monte-Carlo method. The line profile of the photons escaping by the upper window (observation near the center of the solar disk) is the sum of three components:

(i) the radiation that crosses the cylinder without absorption. The corresponding profiles have the same wings as the incident profiles, since the object is optically thin at these frequencies. The line center is depressed by absorption. If the optical thickness is sufficient (cases 1 and 3), the absorption is complete at line center.

(ii) the photons, coming initially from the solar surface, that escape after a number of scatterings. When the optical thickness is significant (cases 1 and 3), the corresponding profile is self-reversed. In the nearly optically thin case 2, it has a quasi-gaussian shape.

(iii) the photons created inside the loop, and possibly scattered before escape. The profile is similar to that of the preceding case, but the absolute intensity increases with pressure.

The relative importance of these three components depends on optical thickness and pressure. At low pressures (cases 1 and 2) the resulting profile remains similar to the solar profile, with a relative depression at the center of the line, and possibly a reinforcement of the peaks. At high pressures, collisional processes become preponderant, so that the total profile is similar to the "creation profile", except in the very optically thin wings, where direct transmission dominates. The mechanism of line formation for photons escaping by the side window (observations at the limb) is similar but limited to processes (ii) and (iii). Thus, these profiles drop sharply in the wings, contrary to the preceding ones. They are self-reversed or not according to the optical thickness of the loop.

4.2.2. Transverse variations of intensity

Observed with sufficient angular resolution, coronal loops exhibit variations of intensity transverse to the axis, arising principally from variations of optical depth along the line of sight. For every loop model under study, we obtained these variations for each of the two windows. A sample of these results, illustrating two different cases, is represented in Fig. 10. The first one concerns a low pressure (0.01 dyn cm^{-2}) loop with a substantial optical depth ($\tau \sim 100$) at the center, which is representative of the scattering-dominated case. These loops appear in absorption on the disk, since the photons absorbed in the core of the line are not balanced by those arising from scattering. The corresponding curve is concave, the minimum of intensity corresponding to the maximum of optical thickness. When looking at the side window, one observes the opposite variation, the thickest parts being the brightest. In a sense, the two curves are complementary, as the scattering removes some part of the upgoing photons to redistribute them horizontally. The second case, which concerns a high pressure (1 dyn cm^{-2}) loop with low optical depth ($\tau \sim 4$), is characteristic of the collision-dominated case. The curves of

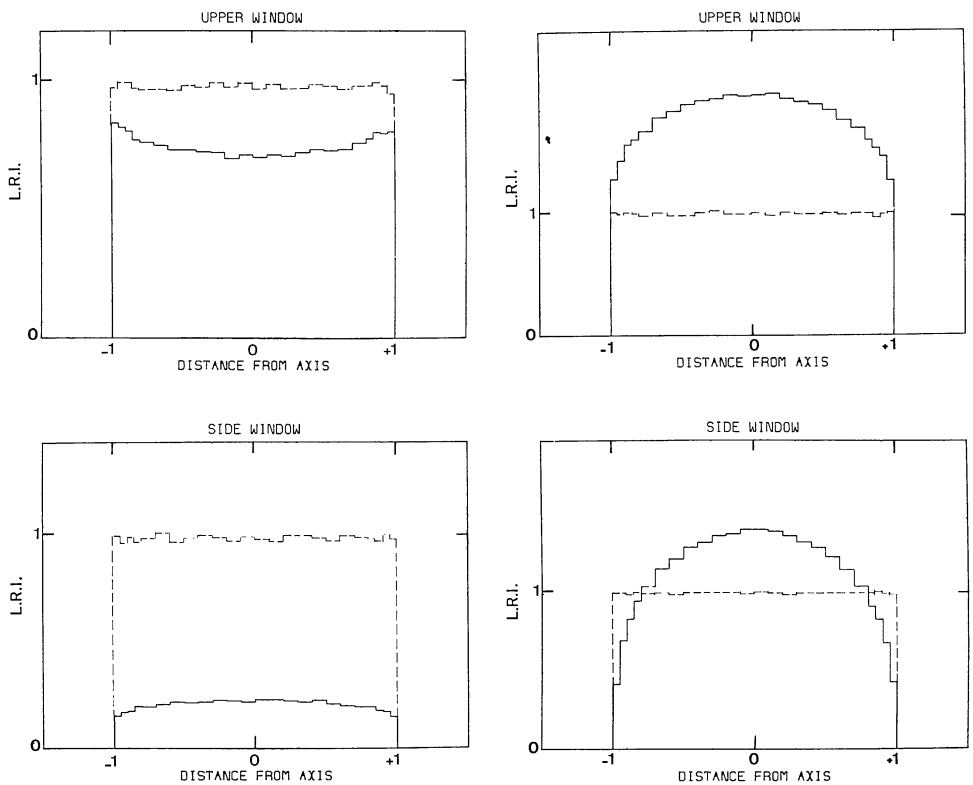

Fig. 10. Transversal variations of intensities (LRI) emitted by cylinders. *Left:* $p = 0.01$ dyn cm^{-2}, $T = 20000$ K. *Right:* $p = 1$ dyn cm^{-2}, $T = 70000$ K. *Top:* observation by the upper window. *Bottom:* observation by the side window. The distance from axis is in Mm. The solid lines represent the emission by the cylinder, and the dotted lines the solar disk's reference (constant except statistical noise)

© European Southern Observatory • Provided by the NASA Astrophysics Data System

1986A&A...154..154G

variation are convex for both directions of emission, since the number of photons produced by internal creation is larger than the number of photons absorbed. These results simply generalize those obtained for optically thin loops in Sect. 2.

4.2.3. Directional diagrams

We also recorded the variations of Lα emission as a function of the direction, represented by two angular coordinates, θ and ϕ. As an example, we have represented in Fig. 11 the variation of intensity as a function of ϕ, emitted in a nearly horizontal plane ($90° \leq \theta \leq 105°$), for 3 different loop models. These models correspond to the same pressure (1 dyn cm^{-2}), but have different temperatures, and thus different optical thicknesses. When the optical thickness increases, the emission tends to be isotropic. On the contrary, optically thin cylinders present a reinforcement of emission along the axis.

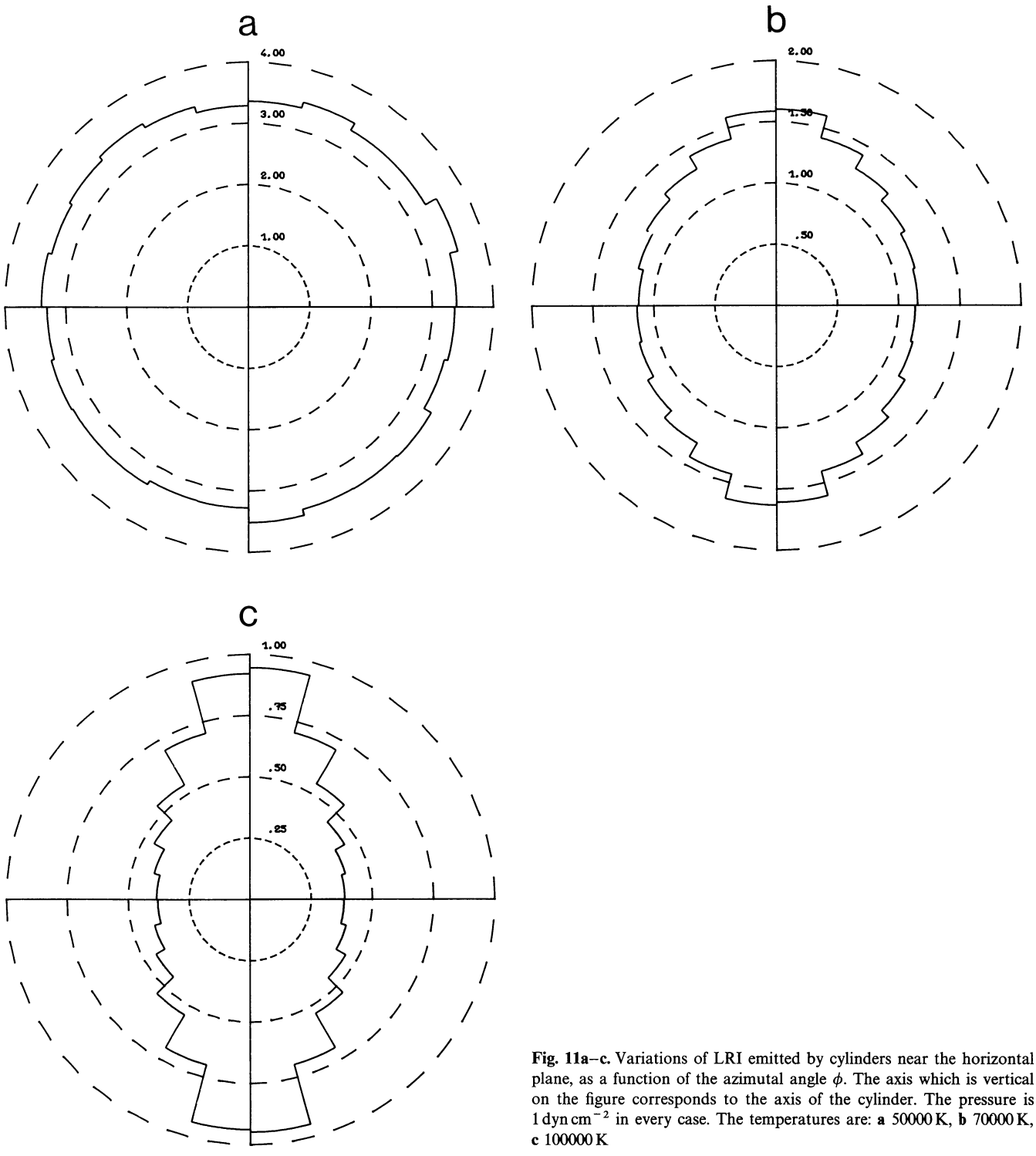

Fig. 11a–c. Variations of LRI emitted by cylinders near the horizontal plane, as a function of the azimutal angle ϕ. The axis which is vertical on the figure corresponds to the axis of the cylinder. The pressure is 1 dyn cm^{-2} in every case. The temperatures are: **a** 50000 K, **b** 70000 K, **c** 100000 K

© European Southern Observatory • Provided by the NASA Astrophysics Data System

1986A&A...154..154G

4.2.4. Validity of plane-parallel models

From the computational point of view, the replacement of a cylinder by a plane-parallel slab with thickness equal to its diameter is very beneficial, since one-dimensional transfer codes can be used. Whereas this procedure may seem a priori unphysical, it gives rather good results, as it may be seen in Fig. 12, where intensities emitted by slabs and cylinders are compared. For low pressures (0.01 and 0.1 dyn cm^{-2}), we find no significant differences between the two kinds of objects, except for $P =$ 0.01 dyn cm^{-2} and $T = 20000$ K, where the emission of the cylinder observed at the limb is higher than that of the vertical slab by about 15%. But it is difficult to determine whether this difference comes from geometrical effects or from the difference in frequency redistribution (complete for the cylinder, partial for the slab). At higher pressures (1 dyn cm^{-2}), more substantial departures may be observed. Here, cylinders have weaker emissions than slabs, and the maximum of the relative difference, about 25%, is reached for $T = 70000$ K, i.e., an optical thickness of about 4. As a tentative explanation, we may propose that the slab geometry ensures a better confinement of radiation than the cylinder geometry and thus increases source functions and intensities.

In spite of its limitations (especially concerning the number of models studied), the present comparison shows the utility of one-dimensional computations in the study of coronal loops and gives an estimate of the errors that can arise from this procedure. In the optically thin region, the emission becomes independent of geometry, as seen in Sect. 2. Towards large optical thicknesses, it remains a lack of comparative computations. Nevertheless, as the curvature per unit optical depth decreases, it is likely that the cylinders behave more and more as slabs from the point of view of radiative transfer.

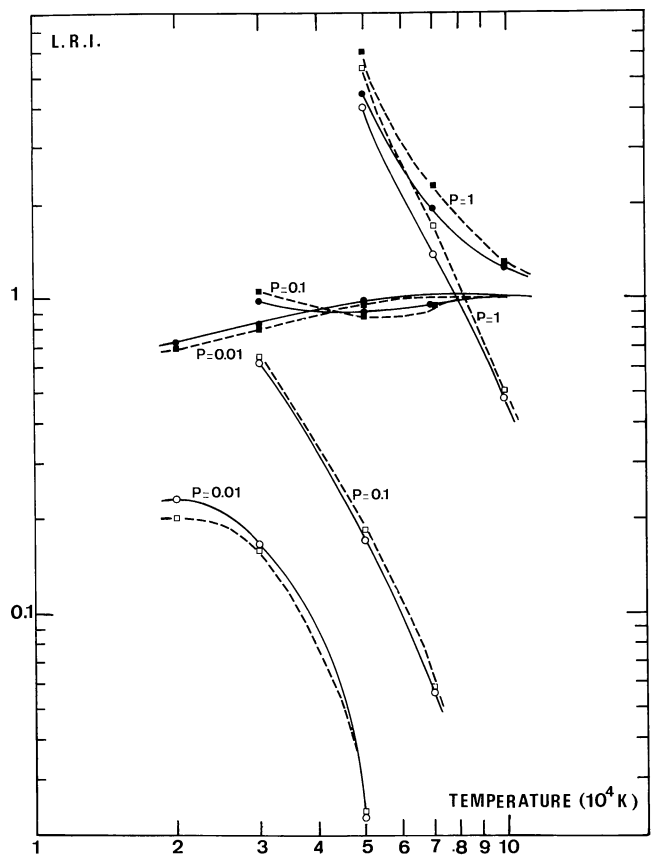

Fig. 12. Comparison of LRI's from cylinders and slabs, as functions of temperature. The pressures are indicated in dyn cm^{-2}. *Open circles*: cylinders observed at limb. *Open squares:* (vertical) slabs at limb. *Full circles:* cylinders on the disk. *Full squares:* (horizontal) slabs on the disk

4. Conclusion

The aim of this paper was to provide some theoretical basis to support the analysis of Lyman-α filtergrams (such as the ones obtained with the Transition Region Camera) and, in particular, the diagnosis of loops that can be seen on these pictures. To reach this objective, we computed the intensities emitted by coronal loops in a wide range of pressures and temperatures. We determined the influence, on the emitted intensities, of the model hydrogen atom and redistribution functions used, and evaluated the possibilities of replacing the cylindrical geometry by a plane-parallel one. In the case of optically thin structures observed at the limb, we find that Lyman-α relative intensities (LRI) are proportional to the pressure when it is low and to its square when it is high. A formula for the LRI as a function of pressure and temperature (and thickness) of the structure is given. The LRI's computed on the disk show a high sensitivity to the pressure. Computations extended to optically thick slabs show non-monotonous variations of the LRI with temperature at a given pressure; in particular, a low contrast on the disk may still be the indication of a very opaque structure at low pressure and temperature. Most results are explained in terms of the relative weight of collisional excitation (between levels 1 and 2) as compared to photon scattering. Finally, the effect of cylindrical geometry, investigated with a Monte-Carlo method, is shown to be marginally important.

Consequently, we think that the present results (and especially the detailed computations performed with the slab geometry) will be useful to determine the possible positions of actually observed loops in a pressure-temperature diagram. Lyman-α filtergrams, such as TRC ones, provide with the geometrical thickness, and LRI's measured on the disk and at the limb. In some extreme cases (LRI lower than 0.2 or higher than a few tens), a pressure/temperature diagnostic may be established. In other ones, more information is necessary, about the opacity for instance: in this respect, the simultaneously observed Hα intensity may help to put an upper limit on the Lα opacity. EUV intensities of metal lines give also accesss to the emission measure from which the electron density can be derived, a supplementary constraint in the pressure-temperature diagram.

The diagrams given in this paper do not replace a specific modeling of a given loop which, on account of the number of parameters involved (pressure, temperature, diameter, velocity, etc.) is altogether necessary in filtergram diagnostic studies. Nevertheless, in such a context, they should be useful to restrict a priori the range of models that can be associated with a given observation.

Acknowledgements. We are grateful to C.E. Alissandrakis and R.M. Bonnet for their valuable help during this work, and for the encouragements they provided us, to P. Heinzel for the fruitful discussions we had together during his stay in L.P.S.P. in

© European Southern Observatory • Provided by the NASA Astrophysics Data System

1986A&A...154..154G

1984 and that contributed to improve substantially this paper, and to P. Lemaire and other members of the L.P.S.P. Solar Physics team who helped us at a moment of this research.

The main part of the computations (on plane-parallel slabs) were done with the Cray-1 computer of the "Centre de Calcul Vectoriel pour la Recherche" (C_2VR). Other computations used the facilities of the "Centre Spatial de Toulouse" (CNES).

References

Adams, T.F., Hummer, D.G., Rybicki, G.B.: 1971, *J. Quant. Spectroscop. Radiat. Transfer* **11**, 1365

Avery, L.W., House, L.L., Skumanich, A.: 1969 *J. Quant. Spectroscop. Radiat. Transfer* **9**, 519

Basri, G.S., Linsky, J.L. Bartoe, J.D.F., Brueckner, G., Van Hoosier, M.E.: 1979, *Astrophys. J.* **230**, 924

Beckers, J.M., Bridges, C.A., Gilliam, L.B.: 1976, "A high resolution spectral atlas of the solar irradiance from 380 to 700 nanometers. Volume 1: Tabular form", Air force Geophysics Laboratory Report AFGL-TR-76-0126 (1)

Bonnet, R.M., Bruner, E.C. Jr., Acton, L.W., Brown, W.A., Decaudin, M.: 1980, *Astrophys. J.* **237**, L47

Bonnet, R.M., Tsiropoula, G.: 1982, *Solar Phys.* **75**, 139

Cashwell, E.D., Everett, C.J.: 1959, "A manual of the Monte Carlo Method for Random Walk Problems", New York: Pergamon

David, K.H.: 1961, *Z. Astrophys.* **53**, 37

Dunn, R.B.: 1971, in "Physics of the solar Corona", ed. C.J. Macris, Dordrecht: Reidel

Feldman, U., Doschek, G.A., Behring, W.E.: 1978, *Space Sci. Rev.* **22**, 191

Foukal, P.: 1975, *Solar Phys.* **43**, 327

Foukal, P.: 1976, *Astrophys. J.* **210**, 575

Foukal, P.: 1978, *Astrophys. J.* **223**, 1046

Gabriel, A.H.: 1971, *Solar Phys.* **21**, 392

Gabriel, A.H., Garton, W.R.S., Goldberg, L., Jones, T.J.L., Jordan, C., Morgan, F.J., Nicholls, R.W., Parkinson, W.J., Paxton, H.J.B., Reeves, E.M., Shenton, C.B., Speer, R.J., Wilson, R.: 1971, *Astrophys. J.* **169**, 595

Heinzel, P.: 1984, Private Communication

Jefferies, J.T.: 1968, Spectral line formation, Waltham: Blaisdell

Johnson, L.C.: 1972, *Astrophys. J.* **174**, 227

Koschmieder, H., Raible, V., Kleinpoppen, H.: 1973, *Phys. Rev. A* **8**, 1365

Lemaire, P., Gouttebroze, P., Vial, J.-C., Artzner, G.: 1981, *Astron. Astrophys.* **103**, 160

Mc Gowan, J.W., Williams, J.F., Curley, E.K.: 1969, *Phys. Rev.* **180**, 132

Rosner, R., Tucker, W.H., Vaiana, G.S.: 1978, *Astrophys. J.* **220**, 643

Tousey, R., Bartoe, J.D.F., Bohlin, J.D., Brueckner, G.E., Purcell, J.D., Scherrer, V.E., Sheeley, N.R. Jr., Schumacher, R.J., Van Hoosier, M.E.: 1973, *Solar Phys.* **33**, 265

Vaiana, G.S.: 1968, *Science* **161**, 564

Vaiana, G.S., Krieger, A.S., Timothy, A.F.: 1973, *Solar Phys.* **32**, 81

Van de Hulst, H.C.: 1953, in "The Sun", ed. G.P. Kuiper, Chicago: Univ. Chicago Press

Vernazza, J.E.: 1972, Ph.D. Thesis, Harvard University

Vernazza, J.E., Reeves, E.M.: 1978, *Astrophys. J. Suppl.* **37**, 485

Vial, J.C.: 1982, *Astrophys. J.* **254**, 780

Williams, J.F., Willis, B.A.: 1974, *J. Phys. B* **7**, L 61

Withbroe, G.L., Kohl, J.L., Weiser, H., Noci, G., Munro, R.H.: 1982, *Astrophys. J.* **254**, 361

© European Southern Observatory • Provided by the NASA Astrophysics Data System